# Evidence for Rapid Adiabatic Cooling as an Origin of the Recombining Plasma in the Supernova Remnant W49B Revealed by *NuSTAR* Observations

Hiroya Yamaguchi[1] , Takaaki Tanaka[2] , Daniel R. Wik[3] , Jeonghee Rho[4,5] , Aya Bamba[6,7] , Daniel Castro[8] , Randall K. Smith[8] , Adam R. Foster[8] , Hiroyuki Uchida[2], Robert Petre[9] , and Brian J. Williams[9]

[1] Institute of Space and Astronautical Science, JAXA, 3-1-1 Yoshinodai, Sagamihara, Kanagawa 229-8510, Japan; yamaguchi@astro.isas.jaxa.jp
[2] Department of Physics, Kyoto University, Kitashirakawa-oiwake-cho, Sakyo-ku, Kyoto 606-8502, Japan
[3] Department of Physics & Astronomy, University of Utah, 115 South 1440 East Salt Lake City, UT 84112, USA
[4] SETI Institute, 189 Bernardo Avenue, Mountain View, CA 94043, USA
[5] SOFIA Science Center, NASA Ames Research Center, MS 232, Moffett Field, CA 94035, USA
[6] Department of Physics, The University of Tokyo, Bunkyo, Tokyo, 113-0033, Japan
[7] Research Center for the Early Universe, School of Science, The University of Tokyo, 7-3-1 Hongo, Bunkyo-ku, Tokyo 113-0033, Japan
[8] Harvard-Smithsonian Center for Astrophysics, 60 Garden Street, Cambridge, MA 02138, USA
[9] NASA Goddard Space Flight Center, Code 662, Greenbelt, MD 20771, USA

## Abstract

X-ray observations of supernova remnants (SNRs) in the last decade have shown that the presence of recombining plasmas is somewhat common in a certain type of object. The SNR W49B is the youngest, hottest, and most highly ionized among such objects, and hence provides crucial information about how the recombination phase is reached during the early evolutionary phase of SNRs. In particular, spectral properties of radiative recombination continuum (RRC) from Fe are the key for constraining the detailed plasma conditions. Here we present imaging and spectral studies of W49B with *Nuclear Spectroscopic Telescope Array* (*NuSTAR*), utilizing the highest-ever sensitivity to the Fe RRC at $\gtrsim 8.8$ keV. We confirm that the Fe RRC is most prominent at the western part of the SNR because of the lowest electron temperature ($\sim 1.2$ keV) achieved there. Our spatially resolved spectral analysis reveals a positive correlation between the electron temperature and the recombination timescale with a uniform initial temperature of $\sim 4$ keV, which is consistent with the rapid adiabatic cooling scenario as an origin of the overionization. This Letter demonstrates *NuSTAR*'s suitability for studies of thermal emission, in addition to hard nonthermal X-rays, from young and middle-aged SNRs.

*Key words:* ISM: individual objects (W49B: G43.3-0.2) – ISM: supernova remnants – radiation mechanisms: thermal – X-rays: ISM

## 1. Introduction

X-ray spectroscopy of supernova remnants (SNRs) allows us to investigate the thermal properties of the shocked gas (both swept-up ambient medium and supernova ejecta), providing a powerful probe for the SNR's environment and evolution history. In the last decade, studies with modern X-ray observatories have shown that a number of middle-aged SNRs contain recombining (overionized) plasmas, where the heavy element ions have been stripped of more electrons than they would be if the plasma is in ionization equilibrium (e.g., IC 443, W28, W44, N49: Yamaguchi et al. 2009; Sawada & Koyama 2012; Uchida et al. 2012, 2015). This fact implies that the presence of the "recombination phase" during the remnant evolution is somewhat common among a certain type of SNRs. Yet, detailed mechanisms that lead to the observed plasma properties are still poorly understood.

The SNR W49B is an extremely intriguing object in both thermal and nonthermal aspects, given that it is the most luminous in Fe K-shell emission (Yamaguchi et al. 2014) and GeV $\gamma$-rays (Abdo et al. 2010; H.E.S.S. Collaboration 2018) among Galactic SNRs. This Letter focuses exclusively on its thermal aspect, whereas Tanaka et al. (2018) present our new results on the nonthermal phenomena. Notably, W49B is the youngest (1000–6000 yr: e.g., Pye et al. 1984; Smith et al. 1985; Zhou & Vink 2018) among the known SNRs in the recombining state, making its plasma extraordinarily hot and highly ionized. Previous *Suzaku* observations detected a strong radiative recombination continuum (RRC) of He-like Fe at $E_{\mathrm{edge}} \approx 8.83$ keV, a key spectral feature to constraining the ionization state and electron temperature (Ozawa et al. 2009). There have been several attempts to determine the spatial distribution of the recombining plasma in W49B using *XMM-Newton* (Miceli et al. 2010) and *Chandra* (Lopez et al. 2013a; Zhou & Vink 2018). Both observations indicated that the degree of overionization is more significant in the west than in the east. However, none of these works constrained the detailed plasma properties based on the realistic spectral modeling using the Fe RRC, because of the low signal-to-noise ratios near and above $E_{\mathrm{edge}}$.

Here, we present deep observations of W49B with *Nuclear Spectroscopic Telescope Array (NuSTAR)* that was recently performed with the aim of revealing the early evolutionary characteristics of the overionized SNRs. Although *NuSTAR* is designed to achieve a good sensitivity and an imaging capability to nonthermal radiation components in the hard ($\gtrsim 10$ keV) X-ray band (including both nonthermal continuum and radioactive decay lines of $^{44}$Ti), the "turnover" of the effective area in comparison to other X-ray telescopes takes place at $\sim 6.5$ keV (Harrison et al. 2013), well below $E_{\mathrm{edge}}$ of the Fe RRC. Moreover, its angular resolution or half-power diameter (HPD; HPD $\approx 1'$) is twice better than that of *Suzaku*, and reasonably smaller than the SNR's angular size ($4' \times 3'$). Utilizing these capabilities, we perform the first spatially resolved spectroscopy of W49B including the Fe RRC component.
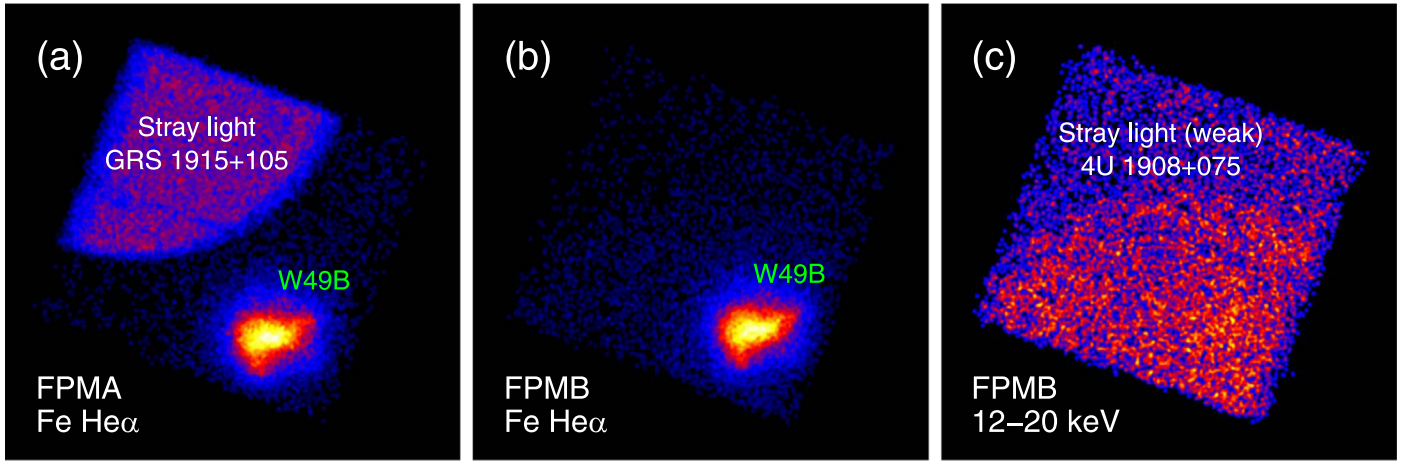
**Figure 1.** Raw photon count images of (a) the FPMA in 6.4–6.8 keV, (b) FPMB in 6.4–6.8 keV, and (c) FPMB in 12–20 keV, in the square root scale. The stray light features from GRS 1915+105 and 4U 1908+075 are detected in the FPMA and FPMB, respectively.

This Letter is organized as follows. In Section 2, we describe details of our *NuSTAR* observations and data reduction. The screened data are analyzed and results are discussed in Section 3. Finally, we conclude this study in Section 4. The errors quoted in the text and table and error bars given in the figures all represent a $1\sigma$ confidence level.

## 2. Observation and Data Reduction

W49B was observed by *NuSTAR* on 2018 March 17–20 (Obs. ID: 40301001002) during Cycle 3 of the Guest Observer Program. We reprocessed the data using the `nupipeline` task in the NuSTARDAS v.1.8.0 software package with the calibration database (CALDB) released on 2018 April 19. We also filtered out periods when the background is high, resulting in the effective exposure of 122 ks. The strictness of our filtering criteria is comparable to that of the `saamode = optimized` and `tentacle = yes` options in the `nupipeline` routine.

Figure 1(a) shows a photon count image of the Focal Plane Module A (FPMA) in the 6.4–6.8 keV band, corresponding to the energies of the Fe He$\alpha$ lines. W49B is observed using the Det 0 chip (bottom right in the figure) where the optical axis is located. The strong stray light from the black hole binary GRS 1915+105 is detected at the off-source regions, which does not affect the analysis of W49B. Figures 1(b) and (c) are FPMB images in 6.4–6.8 keV and 12–20 keV, respectively. Unlike the FPMA, the on-axis Det 0 chip suffers from the stray light from the high mass X-ray binary 4U 1908+075. However, its flux level is relatively low, so the feature is visible only in the hard X-ray band. We appropriately take into account this stray light effect in the subsequent background estimate and spectral analysis.

## 3. Results and Discussion

In Figure 2, we show an image of the Fe RRC-to-He$\alpha$ flux ratio, which is generated by dividing the exposure-corrected image in 8.8–10 keV by that in 6.4–6.8 keV and merging the data from the FPMA and FPMB. An enhancement of the Fe RRC (implying a large degree of overionization) is found at the west rim, consistent with the previous observations (Miceli et al. 2010). For more quantitative study, we analyze spectra from two representative regions, east and west, labeled in Figure 2. The background spectra, consisting of instrumental
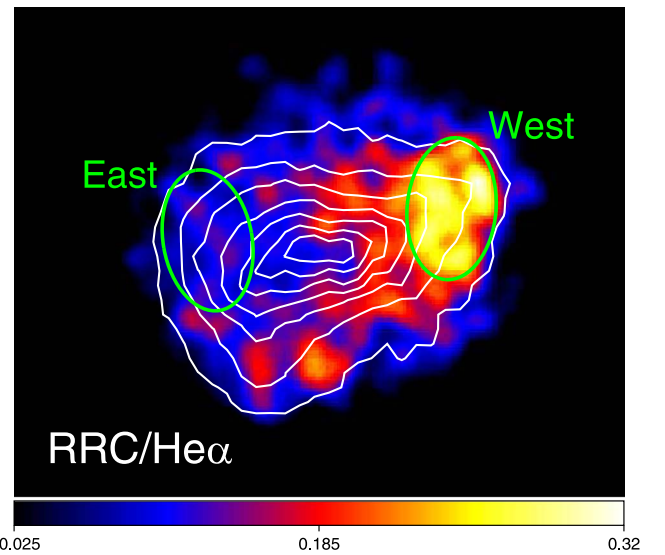


**Figure 2.** Spatial distribution of the flux ratio between the Fe RRC (8.8–10 keV) and Fe He$\alpha$ (6.4–6.8 keV) given in the linear scale. The ratios from the FPMA and FPMB are averaged and then smoothed. The overplotted contours are the exposure-corrected Fe He$\alpha$ flux image. The green ellipses indicate where the spectra shown in Figure 3 are extracted.

background, unresolved X-ray background, and stray light components, are generated using the `nuskybgd` script, whose details are described in Wik et al. (2014).

The spectra of the FPMA (black) and FPMB (red) from each source region are given in Figure 3. The gray and magenta data points are the background spectra generated for the FPMA and FPMB, respectively, the latter showing the higher flux due to the stray light from 4U 1908+075. The prominent RRC is confirmed in the west spectra (Figure 3(b)), whose peak height is, surprisingly, comparable to that of the emission at $\sim$7.8 keV (a mixture of Fe He$\beta$ and Ni He$\alpha$ lines). Moreover, the RRC has a steeper slope in the west, suggesting that a lower electron temperature is achieved there. To verify this, we fit the spectra with a recombining plasma model, `vvrnei` in the XSPEC package (Arnaud 1996), based on the latest atomic database AtomDB version 3.0.9.[10] The important parameters are the current electron temperature ($kT_e$), the initial temperature

---

[10] http://www.atomdb.org
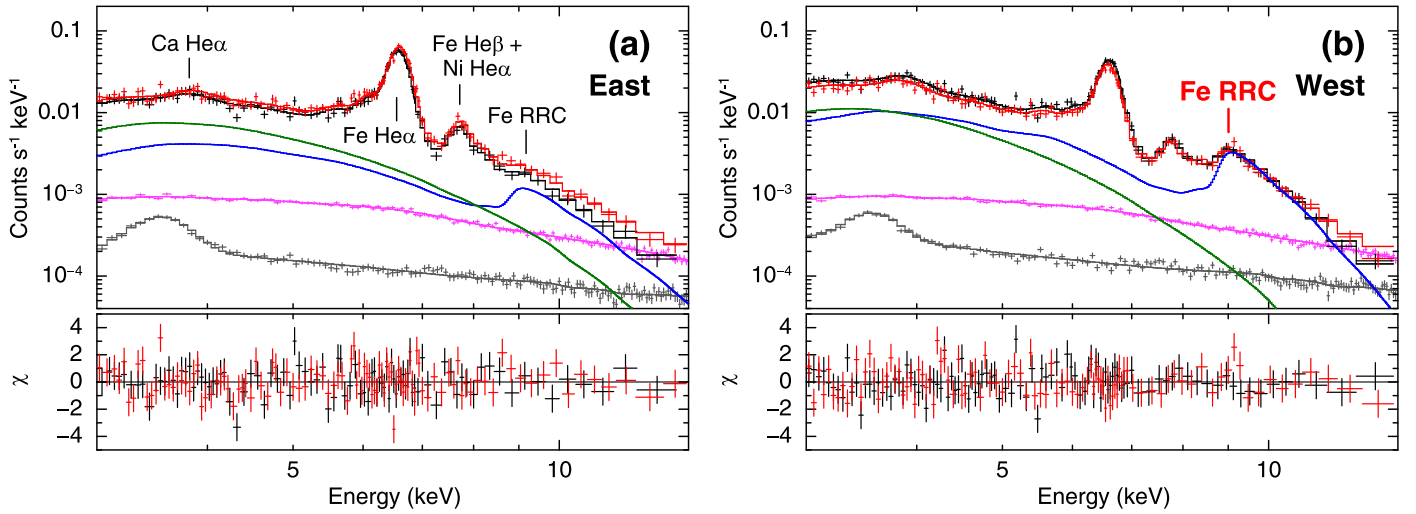
**Figure 3.** *NuSTAR* spectra of the east (a) and west (b), whose locations are given in Figure 2. Black and red are the FPMA and FPMB, respectively. The lower panels show residuals from the best-fit models obtained using the C statistic method, where the background data generated with the `nuskybgd` script (gray and magenta for the FPMA and FPMB, respectively) are simultaneously fitted with the source data. The spectra are rebinned for clarity, although unbinned data are used in the actual analysis. The green and blue curves indicate the contributions of the bremsstrahlung from H and He and the RRCs from heavy elements (C–Ni), respectively, to the FPMA spectra.

**Table 1**
**Best-fit Spectral Parameters**

| Parameter | East | | West | |
|---|---|---|---|---|
| | $\chi^2$ | c-stat | $\chi^2$ | c-stat |
| $kT_e$ (keV) | $1.84 \pm 0.05$ | $1.86 \pm 0.05$ | $1.20 \pm 0.04$ | $1.19 \pm 0.04$ |
| $kT_{init}$ (keV) | $4.77 \pm 0.25$ | 4.77 (fixed)[a] | $3.80^{+0.80}_{-0.54}$ | $3.73^{+0.69}_{-0.49}$ |
| $n_e t$ ($10^{11}$ cm$^{-3}$ s) | $6.32^{+0.43}_{-0.34}$ | $6.12^{+0.32}_{-0.25}$ | $1.83^{+1.65}_{-1.54}$ | $1.66^{+1.47}_{-1.45}$ |
| Ca (solar)[b] | $3.9 \pm 0.8$ | $3.7 \pm 0.8$ | $3.7 \pm 0.5$ | $3.5 \pm 0.5$ |
| Cr (solar)[b] | $12 \pm 3$ | $12 \pm 3$ | $5.1^{+2.0}_{-1.8}$ | $5.8^{+2.0}_{-1.8}$ |
| Mn (solar)[b] | $69 \pm 8$ | $67 \pm 8$ | $20 \pm 4$ | $21 \pm 4$ |
| Fe (solar)[b] | $6.4 \pm 0.4$ | $6.1 \pm 0.4$ | $2.2 \pm 0.4$ | $2.2 \pm 0.4$ |
| Ni (solar)[b] | $13 \pm 3$ | $13 \pm 3$ | $3.3^{+1.4}_{-1.2}$ | $3.4^{+1.4}_{-1.2}$ |
| Norm FPMA[c] | $8.09 \pm 0.33$ | $8.17 \pm 0.33$ | $31.5 \pm 1.6$ | $32.5 \pm 1.6$ |
| Norm FPMB[c] | $9.38 \pm 0.38$ | $9.56 \pm 0.39$ | $30.9 \pm 1.6$ | $32.2 \pm 1.6$ |
| Offset FPMA (ch)[d] | $-2.05$ | $-2.00$ | $-1.23$ | $-1.15$ |
| Offset FPMB (ch)[d] | $-1.48$ | $-1.45$ | $-1.90$ | $-1.73$ |
| $\chi^2$ | 291 | 1058 | 250 | 1009 |
| c-stat | ... | 1010 | ... | 1064 |
| dof. | 267 | 968 | 260 | 969 |

**Notes.** "$\chi^2$" and "c-stat" in the second row indicate the statistical methods of chi-squared and C statistic, respectively.
[a] Fixed to the best-fit value from the $\chi^2$ method, because otherwise the value is not constrained at all.
[b] Values relative to the solar abundances of Wilms et al. (2000).
[c] Normalizations are independently fitted for the FPMA and FPMB. The unit is $10^{-17}/(4\pi D^2) \cdot \int n_e n_H dV$ (cm$^{-5}$), where $D$ is the distance to the source, and $\int n_e n_H dV$ is the volume emission measure.
[d] In *NuSTAR*, the width of each single pulse-height channel corresponds to the photon energy of 40 eV.

($kT_{init}$) that determines the ionization balance before the abrupt plasma cooling, the recombination timescale ($n_e t$) that is the product of the electron density ($n_e$), and the time elapsed after the abrupt cooling ($t$). Other free parameters are all listed in Table 1. Abundances of unlisted heavy elements (e.g., Si, S) are fixed to the solar values of Wilms et al. (2000). Normalizations of the FPMA and FPMB are fitted independently, following the instructions by the *NuSTAR* Science Operations Center (SOC).[11] A foreground absorption is accounted for using the `tbabs` model (Wilms et al. 2000) with a fixed hydrogen column density

of $5 \times 10^{22}$ cm$^{-2}$ (Keohane et al. 2007). We also try a larger value of $8 \times 10^{22}$ cm$^{-2}$, which was reported in more recent work (Lopez et al. 2013b), and find that this difference does not substantially affect our results. Finally, we allow for an offset in the photon energy to the pulse-height relationship to account for possible gain calibration uncertainties.

The spectral fitting with the model described above is performed using two different statistical methods: (1) chi-squared ($\chi^2$) statistic on background-subtracted, binned spectra, and (2) C statistic on background-unsubtracted, unbinned spectra (Cash 1979). For the latter, the background spectra are modeled by phenomenological functions and
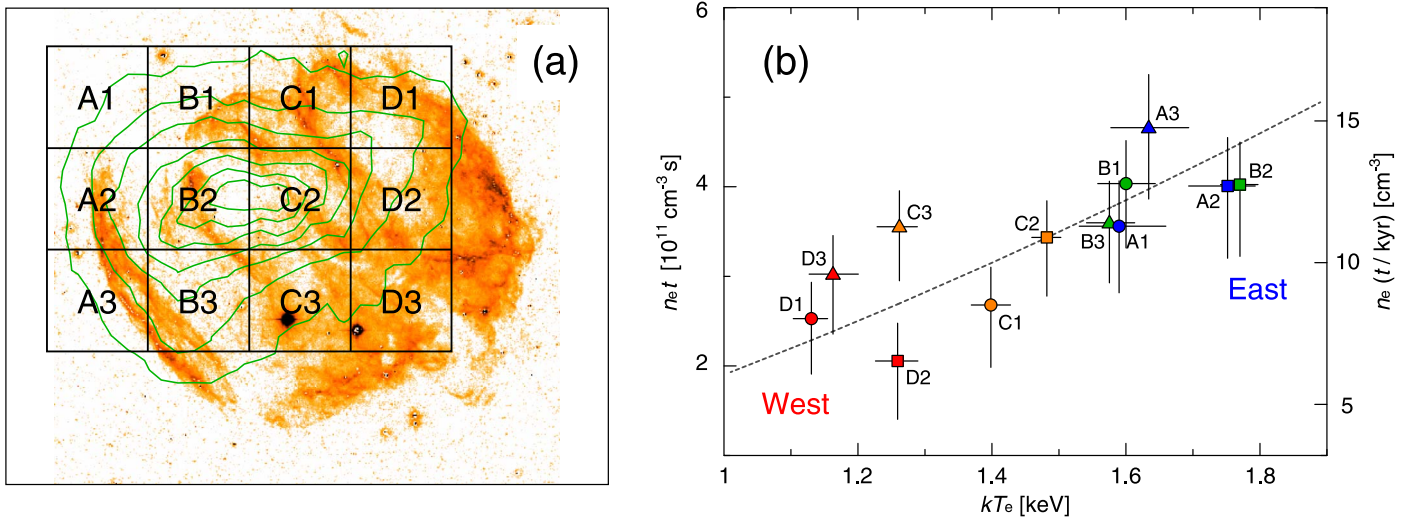
**Figure 4.** (a) $1' \times 1'$ box regions used for the spatially resolved spectral analysis. The green contours are the exposure-corrected Fe Heα flux map (same as the white contours in Figure 2). The color image is obtained with *WIRC* observations of the 1.64 μm [Fe II] band, where background stars are subtracted using the DAOPHOT method that is described in Rho et al. (2001). (b) Relationship between the electron temperature (bottom) and the recombination timescale (left) or the corresponding electron density (right) obtained from the spatially resolved spectral analysis. The region names labeled near the data points correspond to those given in panel(a). The dashed line is a power-law function with an index of 1.5, whose normalization is fitted to match the data.

simultaneously fitted with the source data. The best-fit results are given in Table 1, which are obtained with reasonable goodness of fit ($\chi^2/\text{dof} < 1.1$). In particular, the Fe RRC features are well reproduced in both regions. We find no significant difference between the results from the two statistical methods.

The low electron temperature and low recombination timescale (hence the substantial overionization) are confirmed at the west. At the observed temperatures, the intermediate-mass elements, such as Si and S, require $n_e t \gtrsim 10^{12}\,\text{cm}^{-3}\,\text{s}$ to achieve an ionization equilibrium (Smith & Hughes 2010). This indicates that these elements are also recombining in this SNR, and thus the continuum emission in the *NuSTAR*'s energy band is dominated by their RRCs particularly at the west. This point is illustrated in Figure 3, where the green and blue curves represent the contributions of the bremsstrahlung from H and He and the RRCs from heavy elements (C to Ni), respectively. The abundances given in Table 1 should, therefore, be regarded as relative values to the intermediate-mass elements (not to H), whose abundances are fixed to the solar values in our analysis. Another noteworthy fact is that the electron temperatures that we have constrained are lower than some previous measurements (2–3 keV: e.g., Miceli et al. 2006; Lopez et al. 2009). This discrepancy can also be explained by the RRC effect; in these previous works, the spectra were modeled by ionization equilibrium plasmas, where the broadband continuum is dominated by the bremsstrahlung. As the bremsstrahlung continuum has no spectral edge in the X-ray band, the attempt to reproduce the RRC-dominant spectrum with equilibrium plasma models may have resulted in the overestimation of the electron temperature. On the other hand, our results are consistent with the electron temperatures of the "hot component" ($kT_h$) measured by Zhou & Vink (2018), where recombining plasma models were used.

We obtain extremely high Mn abundances (Mn/Fe ≈ 10) from both regions, inconsistent with previous work (e.g., Hwang et al. 2000; Zhou & Vink 2018). We suspect that this peculiar result is due to an incomplete calibration of the line spread function, given that the Mn Heα emission lies in the

low-energy tail of the stronger Fe Heα lines. We do not investigate this problem further because it does not affect the measurement of the other parameters, such as the electron temperature and recombination timescale, and because the abundance structure is out of the scope of this Letter.

Finally, we perform spatially resolved spectral analysis by dividing the Fe-rich regions into twelve $1' \times 1'$ boxes (the size comparable to the *NuSTAR*'s HPD) indicated in Figure 4(a), where a 1.64 μm [Fe II] image from *Wide Field Infrared Camera (WIRC)* is also shown. The [Fe II] emission is a dominant cooling line from the interstellar medium with a density of $30$–$10^4\,\text{cm}^{-3}$ and a temperature of $10^3$–$10^5\,\text{K}$ (Hewitt et al. 2009). Given that the best-fit $kT_{\text{init}}$ values for the east and west are comparable to each other ($\sim 4$ keV), we assume a common initial temperature shared over the entire SNR, and fit the 24 spectra (12 regions × 2 modules) simultaneously by linking $kT_{\text{init}}$ among the regions. The other parameters in Table 1 are all independently fitted. This analysis obtains $kT_{\text{init}} = 3.84^{+0.18}_{-0.24}$ keV with $\chi^2/\text{dof} = 2745/2616$. The values of $kT_e$ and $n_e t$ derived for each region are plotted in Figure 4(b), showing a clear correlation between the two quantities. In fact, we obtain a large positive correlation coefficient of 0.78.

The observed correlation suggests that lower electron temperatures are achieved in the lower density regions, qualitatively consistent with a rapid adiabatic expansion scenario as an origin of the overionization (Itoh & Masai 1989; Yamaguchi et al. 2009). This scenario requires dense circumstellar matter (CSM) present close to the pre-explosion massive star, so that both CSM and supernova ejecta get shock heated and highly ionized shortly after the progenitor explosion (Moriya 2012). When the blast wave breaks out into the surrounding low-density region, the plasma cools rapidly (Itoh & Masai 1989; Shimizu et al. 2012). Such density distribution can naturally be explained if the progenitor is a red supergiant (RSG), because the main-sequence wind can form a wind-blown cavity around the dense CSM of the RSG wind (e.g., Dwarkadas 2005). The massive progenitor scenario is also consistent with the presence of the dense wind-blown shell

observed in the infrared image of the [Fe II] emission (Keohane et al. 2007), although a SN Ia origin was recently suggested for this remnant (Zhou & Vink 2018).

In adiabatic processes of an ideal monatomic gas in a closed system, $TV^{\gamma-1}$ is conserved, where $T$, $V$, and $\gamma$ ($=5/3$) are the gas temperature, volume, and adiabatic index, respectively. Therefore, if the uniform temperature ($T_{init}$) and density ($n_{init}$) were achieved in the initially shock-heated materials, and if the rapid adiabatic cooling took place at the same time throughout the SNR, then the relationship $n_e \propto T^{1.5}$ is expected among arbitrary fluid elements that have experienced the cooling. This expectation is confirmed in our spatially resolved spectral analysis. A power-law function with an index of 1.5 (the dashed line in Figure 4(b)) appropriately fits the observed relation between $kT_e$ and $n_e$ (which is derived simply from the recombination timescale), although in reality the SNR would have evolved through more complex paths than our assumptions. For instance, the initial condition ($T_{init}$ and $n_{init}$) might not have been uniform, and $T_e$ and $n_e$ might have changed even after the rapid cooling. Future theoretical work accounting for more realistic SNR evolution, such as those performed by Zhou et al. (2011) and Slavin et al. (2017), would be helpful for detailed comparison between the observed and predicted plasma properties.

Recent studies of several other middle-aged SNRs suggest thermal conduction into the surrounding cold gas as a predominant origin of the overionization, given the fact that the recombining plasmas are localized near the molecular clouds (e.g., G166.0+4.3, W28: Matsumura et al. 2017; Okon et al. 2018). (See also Kawasaki et al. 2005 for the thermal conduction scenario originally applied to W49B based on *ASCA* results.) In W49B, on the other hand, the electron temperature gradually goes down from the east to the west (Figure 4(b)), and the plasma condition does not seem to be correlated with the ambient cold gas density that is represented by the infrared emission (Figure 4(a)). This is another piece of evidence that adiabatic expansion is a more suitable explanation for the plasma overionization observed in this SNR. In fact, previous X-ray observations of W49B indicate a lower ambient density at the west than at the east, so the adiabatic cooling can take place more efficiently at the former (Miceli et al. 2010; Lopez et al. 2013a). The plausibility of this scenario is also confirmed by previous hydrodynamical simulations, where the density structure around this SNR is introduced as an initial condition (Zhou et al. 2011).

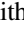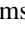## 4. Conclusions

We have presented the *NuSTAR* observations of W49B, focusing on its thermal aspect. A clear enhancement of the Fe RRC is observed at the western part of the SNR. Our spatially resolved spectroscopy has revealed a positive correlation between the electron temperature and the recombination timescale (or the electron density), with a gradient from the west (lower) to the east (higher). The result can naturally be explained when the rapid adiabatic cooling is assumed to be a predominant origin of the overionization. The initial plasma temperature just before the rapid cooling took place ($kT_{init}$) is estimated to be $\sim 4$ keV. There is no spatial correlation between the plasma condition and the ambient cold gas distribution, making the thermal conduction scenario unlikely as a major driver of the rapid cooling in this SNR.

This work has newly expanded the capability of *NuSTAR*. Although this mission has so far focused on *nonthermal* phenomena in SNRs (e.g., Grefenstette et al. 2015, 2017; Lopez et al. 2015), its large effective area and low background in 6–10 keV are remarkably suitable for detecting *thermal* emission in this energy band (i.e., both lines and RRCs from the Fe-peak elements). This advantage can be utilized for observations of other SNRs, such as those emitting strong Ni K$\alpha$ lines (e.g., *Kepler*, 3C 397: Park et al. 2013; Yamaguchi et al. 2015), whose spatial distribution provides crucial information about the SN Ia explosion mechanism. Searching for recombining plasmas in other SNRs (e.g., Bamba et al. 2018) would also be feasible for this observatory.

### ORCID iDs

Hiroya Yamaguchi https://orcid.org/0000-0002-5092-6085
Takaaki Tanaka https://orcid.org/0000-0002-4383-0368
Daniel R. Wik https://orcid.org/0000-0001-9110-2245
Jeonghee Rho https://orcid.org/0000-0003-3643-839X
Aya Bamba https://orcid.org/0000-0003-0890-4920
Daniel Castro https://orcid.org/0000-0002-0394-3173
Randall K. Smith https://orcid.org/0000-0003-4284-4167
Adam R. Foster https://orcid.org/0000-0003-3462-8886
Robert Petre https://orcid.org/0000-0003-3850-2041
Brian J. Williams https://orcid.org/0000-0003-2063-381X

### References

Abdo, A. A., Ackermann, M., Ajello, M., et al. 2010, ApJ, 722, 1303
Arnaud, K. A. 1996, in ASP Conf. Ser. 101, Astronomical Data Analysis Software and Systems V, ed. G. H. Jacoby & J. Barnes (San Francisco, CA: ASP), 17
Bamba, A., Ohira, Y., Yamazaki, R., et al. 2018, ApJ, 854, 71
Cash, W. 1979, ApJ, 228, 939
Dwarkadas, V. V. 2005, ApJ, 630, 892
Grefenstette, B. W., Fryer, C. L., Harrison, F. A., et al. 2017, ApJ, 834, 19
Grefenstette, B. W., Reynolds, S. P., Harrison, F. A., et al. 2015, ApJ, 802, 15
Harrison, F. A., Craig, W. W., Christensen, F. E., et al. 2013, ApJ, 770, 103
H.E.S.S. Collaboration 2018, A&A, 612, A5
Hewitt, J. W., Rho, J., Andersen, M., & Reach, W. T. 2009, ApJ, 694, 1266
Hwang, U., Petre, R., & Hughes, J. P. 2000, ApJ, 532, 970
Itoh, H., & Masai, K. 1989, MNRAS, 236, 885
Kawasaki, M., Ozaki, M., Nagase, F., Inoue, H., & Petre, R. 2005, ApJ, 631, 935
Keohane, J. W., Reach, W. T., Rho, J., & Jarrett, T. H. 2007, ApJ, 654, 938

Lopez, L. A., Grefenstette, B. W., Reynolds, S. P., et al. 2015, ApJ, 814, 132
Lopez, L. A., Pearson, S., Ramirez-Ruiz, E., et al. 2013a, ApJ, 777, 145
Lopez, L. A., Ramirez-Ruiz, E., Castro, D., & Pearson, S. 2013b, ApJ, 764, 50
Lopez, L. A., Ramirez-Ruiz, E., Pooley, D. A., & Jeltema, T. E. 2009, ApJ, 691, 875
Matsumura, H., Uchida, H., Tanaka, T., et al. 2017, PASJ, 69, 30
Miceli, M., Bocchino, F., Decourchelle, A., Ballet, J., & Reale, F. 2010, A&A, 514, L2
Miceli, M., Decourchelle, A., Ballet, J., et al. 2006, A&A, 453, 567
Moriya, T. J. 2012, ApJL, 750, L13
Okon, H., Uchida, H., Tanaka, T., Matsumura, H., & Tsuru, T. G. 2018, PASJ, 70, 35
Ozawa, M., Koyama, K., Yamaguchi, H., Masai, K., & Tamagawa, T. 2009, ApJL, 706, L71
Park, S., Badenes, C., Mori, K., et al. 2013, ApJL, 767, L10
Pye, J. P., Becker, R. H., Seward, F. D., & Thomas, N. 1984, MNRAS, 207, 649

Rho, J., Jarrett, T. H., Cutri, R. M., & Reach, W. T. 2001, ApJ, 547, 885
Sawada, M., & Koyama, K. 2012, PASJ, 64, 81
Shimizu, T., Masai, K., & Koyama, K. 2012, PASJ, 64, 24
Slavin, J. D., Smith, R. K., Foster, A., et al. 2017, ApJ, 846, 77
Smith, A., Jones, L. R., Peacock, A., & Pye, J. P. 1985, ApJ, 296, 469
Smith, R. K., & Hughes, J. P. 2010, ApJ, 718, 583
Tanaka, T., Yamaguchi, H., Wik, D. R., et al. 2018, arXiv:1810.07036
Uchida, H., Koyama, K., Yamaguchi, H., et al. 2012, PASJ, 64, 141
Uchida, H., Koyama, K., & Yamaguchi, H. 2015, ApJ, 808, 77
Wik, D. R., Hornstrup, A., Molendi, S., et al. 2014, ApJ, 792, 48
Wilms, J., Allen, A., & McCray, R. 2000, ApJ, 542, 914
Yamaguchi, H., Badenes, C., Foster, A. R., et al. 2015, ApJL, 801, L31
Yamaguchi, H., Badenes, C., Petre, R., et al. 2014, ApJL, 785, L27
Yamaguchi, H., Ozawa, M., Koyama, K., et al. 2009, ApJL, 705, L6
Zhou, P., & Vink, J. 2018, A&A, 615, A150
Zhou, X., Miceli, M., Bocchino, F., et al. 2011, MNRAS, 415, 244